


## Tunable multi-frequency exceptional points in non-Hermitian terahertz metasurfaces

Xiang Hou(侯翔), Fangze Deng(邓方泽), Zhihua Han(韩志华), Yumeng Ma(马宇萌), Chenglong Wang(王成龙), Yuchao Li(李玉超), Keke Cheng(程可可), Ke Ma(马克), Yansheng Shao(邵延胜), Ruidan Zhou(周瑞丹), Yuping Zhang(张玉萍), Meng Liu(刘蒙), and Huiyun Zhang(张会云)

**Citation:**Chin. Phys. B, 2026, 35 (**5**): 057802. DOI: 10.1088/1674-1056/ae12d8
http://cpb.iphy.ac.cn; http://iopscience.iop.org/cpb

**What follows is a list of articles you may be interested in**

---

## Piezo-phototronic effect on intersubband optical absorption in ZnO/MgZnO quantum wells

Yuchang Liu(刘羽畅), Jiuzhou Chen(陈九州), Yonglong Yang(杨永龙), Xiaolong Pan(潘小龙), Xin Xue(薛鑫), Minjiang Dan(但敏江), Zhengwei Xiong(熊政伟), and Zhipeng Gao(高志鹏)

Chin. Phys. B, 2025, 34 (**8**): 087802. DOI: 10.1088/1674-1056/adce93

## Probing photocarrier dynamics of pressurized graphene using time-resolved terahertz spectroscopy

Yunfeng Wang(王云峰), Shujuan Xu(许淑娟), Jin Yang(杨金), and Fuhai Su(苏付海)

Chin. Phys. B, 2023, 32 (**6**): 067802. DOI: 10.1088/1674-1056/acc2b1

## Graphene metasurface-based switchable terahertz half-/quarter-wave plate with a broad bandwidth

Xiaoqing Luo(罗小青), Juan Luo(罗娟), Fangrong Hu(胡放荣), and Guangyuan Li(李光元)

Chin. Phys. B, 2023, 32 (**2**): 027801. DOI: 10.1088/1674-1056/ac80a8

## Dynamically controlled asymmetric transmission of linearly polarized waves in $VO_2$-integrated Dirac semimetal metamaterials

Man Xu(许曼), Xiaona Yin(殷晓娜), Jingjing Huang(黄晶晶), Meng Liu(刘蒙), Huiyun Zhang(张会云), and Yuping Zhang(张玉萍)

Chin. Phys. B, 2022, 31 (**6**): 067802. DOI: 10.1088/1674-1056/ac4bd3

## Optically tuned dielectric characteristics of $SrTiO_3$/Si thin film in the terahertz range

Bin Zou(邹斌), Qing-Qing Li(李晴晴), Yu-Ping Yang(杨玉平), and Hai-Zhong Guo(郭海中)

Chin. Phys. B, 2021, 30 (**10**): 107802. DOI: 10.1088/1674-1056/ac04a7

---

# Tunable multi-frequency exceptional points in non-Hermitian terahertz metasurfaces

Xiang Hou(侯翔), Fangze Deng(邓方泽), Zhihua Han(韩志华), Yumeng Ma(马宇萌), Chenglong Wang(王成龙), Yuchao Li(李玉超), Keke Cheng(程可可), Ke Ma(马克), Yansheng Shao(邵延胜), Ruidan Zhou(周瑞丹), Yuping Zhang(张玉萍), Meng Liu(刘蒙)[†], and Huiyun Zhang(张会云)[‡]

*Qingdao Key Laboratory of Terahertz Technology, College of Electronic and Information Engineering, Shandong University of Science and Technology, Qingdao* 266590, *China*

(Received 21 August 2025; revised manuscript received 7 October 2025; accepted manuscript online 14 October 2025)

Exceptional points (EPs) in non-Hermitian metasurfaces have garnered considerable attention due to their unique advantages in cutting-edge applications such as ultra-sensitive sensing and unidirectional reflectionlessness. However, existing studies on metasurfaces employing both active and passive tuning mechanisms can only observe a single EP, which fails to meet the requirements for multi-frequency responses or multifunctional integration, thus limiting the enhancement of device performance. In this study, we design a terahertz (THz) non-Hermitian metasurface device that is actively tuned by the phase-change material $VO_2$. By keeping the geometric dimensions of the device unchanged, we achieve the simultaneous induction and detection of multi-frequency EPs at multiple frequency points. Through the regulation of $VO_2$ conductivity, the gain–loss distribution of the system can be continuously controlled, leading to the degeneracy of eigenvalues and eigenstates across multiple discrete frequency bands, thereby forming multi-frequency EPs. Furthermore, the design of chiral structures demonstrates that, under identical conductivity conditions, the eigenstates of the original metasurface structure and its chiral counterpart can degenerate into circularly polarized states with opposite rotations, enabling the switching of polarization chirality. These results illustrate that the deep integration of phase-change materials, non-Hermitian photonics, and electromagnetic manipulation in metasurfaces provides a novel design paradigm for the dynamic regulation of multi-frequency EPs and circular polarization control, laying a foundation for the development of high-performance and multifunctional integrated photonic platforms in the THz regime.

**Keywords:** exceptional points, terahertz, non-Hermitian, metasurfaces

**PACS:** 78.67.Pt, 42.25.Ja

**DOI:** 10.1088/1674-1056/ae12d8 **CSTR:** 32038.14.CPB.ae12d8

## 1. Introduction

Non-Hermitian systems have garnered extensive attention in recent years due to their unique physical behaviors in open quantum systems, optical gain media, and dissipative structures. In 1998, Bender and Boettcher introduced parity–time (PT) symmetry into non-Hermitian Hamiltonians, demonstrating that these systems can possess entirely real eigenvalues when the Hamiltonian commutes with the PT combined operator, thereby providing a new perspective for studying non-Hermitian systems.[1] In quantum mechanics, the Hamiltonian is typically required to be Hermitian to ensure that the energy eigenvalues of the system are real. However, in open systems, the inevitable coupling between gain and loss leads to a deviation from Hermiticity, encompassing systems such as laser cavities,[2] optical gain devices,[3] and integrated electronic devices.[4] PT-symmetric systems can undergo a phase transition from the symmetric phase to the broken phase as system parameters vary. When the system is in the PT-symmetric phase, the eigenvalues exhibit Hermiticity with no imaginary parts, and the eigenstates manifest as elliptically polarized states with major axes oriented at $\pm 45°$. In contrast, when the system is in the PT-broken phase, the real parts of the eigenvalues become degenerate, while the imaginary parts are conjugate, and the eigenstates appear as elliptically polarized states with major axes oriented at $0°$ and $90°$.[5–9] The transition point from the symmetric phase to the broken phase is referred to as the exceptional point (EP). An EP is a degeneracy point in non-Hermitian systems, where both the eigenvalues and the eigenstates are degenerate, resulting in circularly polarized states. This phenomenon exhibits a range of non-trivial effects, including eigenmode merging, geometric phase singularities, and strong non-reciprocity. When circularly polarized light is incident on the metasurface, a phase jump of $\pi$ occurs at the EP. This phase transition characteristic is frequently utilized in sensing and related applications.[10] In recent years, EP-related effects have been extensively applied across various physical platforms, including acoustic cavities,[11] electronic circuits,[12] micro-ring resonators,[13] photonics,[14] ion cavities,[15] and quantum devices,[16] demonstrating significant potential for

[†]Corresponding author. E-mail: liumeng@sdust.edu.cn

[‡]Corresponding author. E-mail: sdust_thz@126.com

© 2026 Chinese Physical Society and IOP Publishing Ltd. All rights, including for text and data mining, AI training, and similar technologies, are reserved.

breakthrough power oscillations,[17] unidirectional invisibility control,[18] coherent perfect absorption,[19] and laser absorption.[20] Similar EP-induced mode hybridization has also been reported in acoustic platforms,[21] underscoring the universality of non-Hermitian degeneracies across various wave systems.

Metasurfaces are a class of two-dimensional artificial interface materials composed of subwavelength structural units. Through meticulous design of their unit cells, the electromagnetic wave properties, including phase, amplitude, and polarization, can be flexibly manipulated at the subwavelength scale.[22] Unidirectional negative refraction has been achieved in PT-symmetric acoustic metasurfaces operating around EPs,[23] thereby demonstrating the unique wave manipulation capabilities facilitated by non-Hermitian physics. The incorporation of non-Hermitian photonics into metasurface design facilitates the realization of EPs and broadens their application dimensions, while simultaneously providing an ideal platform for non-Hermitian photonics. In the terahertz (THz) frequency range, Lawrence *et al*. constructed an anisotropic THz metasurface based on orthogonally coupled resonant elements. This design achieved PT symmetry breaking and a phase transition in the eigenpolarization states by adjusting the structural spacing.[24] Li *et al*. designed a graphene-based split-ring resonator THz metasurface, which dynamically regulates the EP and enables sensitive sensing by controlling the graphene Fermi level to modulate the resonant coupling.[25] He *et al*. developed an amorphous germanium-based THz non-Hermitian metasurface that realizes ultrafast dynamic modulation of the EP and a switchable quarter-wave plate by controlling the loss variation induced by optical pumping, thereby opening up new possibilities for THz components.[26] Further work by He *et al*., utilizing optical pumping-induced loss modulation, achieved EP tuning and chiral inversion on a picosecond timescale, significantly advancing breakthroughs in the modulation speed and functionality of THz non-Hermitian metasurfaces.[27] Although current research has enabled the observation and manipulation of EPs in THz non-Hermitian metasurface structures, existing studies primarily focus on the construction and response mechanisms of single-frequency EPs. No reports have yet demonstrated the simultaneous induction and control of multi-frequency EPs. This limitation to single-frequency operation fails to meet the practical demands of future integrated photonic devices for multi-channel and multifunctional responses.

In this study, we designed a THz non-Hermitian metasurface with active tuning based on the phase-change material $VO_2$. The structure comprises two open-ring resonators made of different materials (gold and chromium) but with identical geometric dimensions, along with a metallic rod positioned between the two open-ring resonators. By regulating the conductivity of $VO_2$ through external excitation, we achieve continuous adjustment of the gain–loss distribution within the coupled system formed by the open-ring resonators and the metallic rod in the metasurface. The conductivity of gold and chromium differs by approximately one order of magnitude in the THz frequency range, enabling the structure to inherently introduce high- and low-loss channels without altering the resonance conditions. Combining this with the reversible phase transition of $VO_2$, we simultaneously induce and observe the degeneracy of eigenvalues and eigenstates at multiple discrete frequency bands, thereby demonstrating the existence of multi-frequency EPs on a single metasurface. This also exhibits multi-frequency EP characteristics, such as a $2\pi$ geometric phase wrapping and asymmetric transmission of circular polarization states. Furthermore, the chiral design of the structure facilitates the switching between circular polarization states with opposite spin at the same conductivity, enhancing the capability for polarization handedness control. This research not only expands the realization dimensions of EPs in THz metasurfaces but also provides a novel design paradigm for multi-frequency, reconfigurable non-Hermitian photonic devices based on phase-change materials.

## 2. Structural design and theoretical analysis

Figures 1(a) and 1(b) illustrate the unit cell of the designed THz non-Hermitian metasurface, organized in a periodic array with lattice constants $P_x = P_y = 160$ μm. The metasurface unit cell consists of three metallic resonant elements: a central metallic rod and a pair of open-ring resonators, made of gold and chromium, respectively. These resonators have identical dimensions but differ in their opening sizes. The gold–chromium dual-metal design capitalizes on the significant disparity in their conductivities, thereby introducing high- and low-loss channels. This configuration facilitates gain/loss imbalance, which is essential for achieving multi-frequency EPs. $VO_2$ thin films are integrated at the openings of the resonators to provide tunable non-Hermitian gain–loss characteristics. The substrate utilized is $SiO_2$, characterized by a relative permittivity of 3.9. The dimensions of the metasurface unit cell are as follows: $L = 117$ μm, $a = 39.5$ μm, $w = 5$ μm, $s = 4$ μm, $n = 8$ μm, $g_1 = 10.3$ μm, and $g_2 = 13$ μm. The thicknesses of the metallic rod, gold open-ring resonator, and chromium open-ring resonator are 0.5 μm, while those of $SiO_2$ and $VO_2$ are 64 μm and 0.55 μm, respectively. Commercial finite-difference time-domain software, CST Microwave Studio, was employed for modeling, and simulations were conducted using the frequency-domain solver.

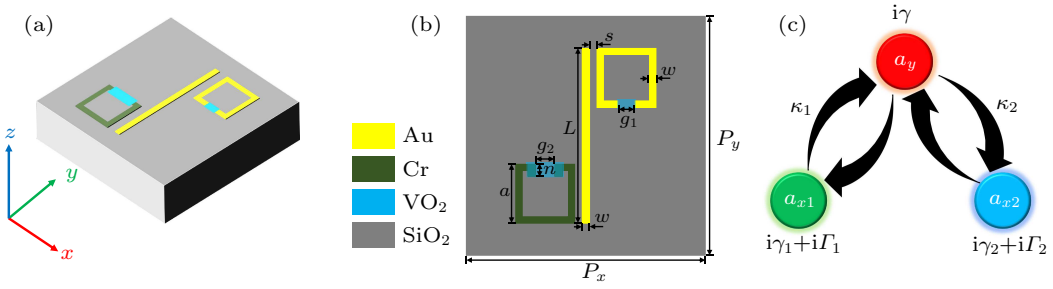



**Fig. 1.** (a) Schematic diagram of the metasurface unit cell structure. (b) Top view of the metasurface unit cell structure. (c) Physical model illustrating the three coupled resonant modes.

$VO_2$, a typical controllable phase-change material, exhibits highly sensitive electrical conductivity in response to temperature variations. This property provides a crucial means for precisely tuning the non-Hermitian characteristics of the system, enabling dynamic control of EPs. Its phase transition behavior manifests as a continuous and reversible transition from an insulating state to a metallic state within a specific temperature range, displaying a diffuse phase transition characteristic.[28] This attribute allows $VO_2$ to achieve smooth modulation of the system's loss parameters without introducing abrupt changes, thereby facilitating precise tuning of the asymmetric loss relationships in the coupling modes between each open-ring resonator and the metallic rod. By adjusting the conductivity of $VO_2$, the system can be effectively driven across the non-Hermitian phase transition boundary, thus facilitating the induction and control of EPs. We employ the Drude model to accurately describe the complex dielectric function of $VO_2$ at varying conductivities in the THz regime:[29]

$$\varepsilon(\omega) = \varepsilon_\infty - \frac{\omega_p^2(\sigma)}{\omega^2 + i\rho\omega}. \tag{1}$$

Here, $\varepsilon_\infty = 12$ is the permittivity at the infinite frequency, $\rho = 5.75 \times 10^{13}$ rad$\cdot$s$^{-1}$ is the collision frequency, $\sigma$ is the electrical conductivity of $VO_2$, which varies with temperature from 20 S$\cdot$m$^{-1}$ to $2 \times 10^5$ S$\cdot$m$^{-1}$, and $\omega_p(\sigma)$ is the plasma frequency, satisfying $\omega_p^2(\sigma) = (\sigma/\sigma_0)\cdot\omega_p^2(\sigma_0)$, where $\sigma_0 = 3 \times 10^5$ S$\cdot$m$^{-1}$ and $\omega_p(\sigma_0) = 1.4 \times 10^{15}$ rad$\cdot$s$^{-1}$. In this study, we emphasize that $VO_2$ is not limited to its fully insulating or metallic states. Instead, we utilize its intermediate transition state, where the electrical conductivity varies continuously from approximately $10^2$ S$\cdot$m$^{-1}$ to $10^5$ S$\cdot$m$^{-1}$. This gradual transition allows for fine and reversible control over the loss distribution without abrupt changes, which is essential for accurately locating and tuning multiple EPs at discrete frequency bands.

As illustrated in Fig. 1(c), the metasurface unit cell exhibits a dipole resonance mode ($a_y$) contributed by the metallic rod oriented in the $y$-direction, along with dual modes ($a_{x_1}$ and $a_{x_2}$) contributed by the two open-ring resonators aligned in the $x$-direction. Unlike conventional dual-resonator designs, the introduction of a third resonator does not aim to create a higher-order EP. Instead, it provides multiple coupling pathways, specifically $a_{x_1} \leftrightarrow a_y$ and $a_y \leftrightarrow a_{x_2}$. Due to differences in geometry ($g_1 \neq g_2$) and material losses (gold and chromium) between these two pathways, their coupling strengths and loss rates vary with frequency. Consequently, each pathway independently meets the second-order EP condition at distinct frequencies, resulting in multi-frequency EPs that are unattainable with traditional dual-resonator systems. The incident light field is a linearly polarized THz wave, the frequency-domain steady-state equations for the modes system, derived from the time-domain dynamical equations through Fourier transform, are expressed as follows:[27]

$$\begin{aligned} j\omega a_{x_1} &= (j\omega_{x_1} - \gamma_{x_1} - \Gamma_{x_1})a_{x_1} \\ &\quad + j\kappa_1 a_y - \sqrt{\gamma_{x_1}\gamma_{x_2}}a_{x_2} + j\sqrt{\gamma_{x_1}}E_x^{in}, \end{aligned} \tag{2}$$

$$\begin{aligned} j\omega a_{x_2} &= (j\omega_{x_2} - \gamma_{x_2} - \Gamma_{x_2})a_{x_2} \\ &\quad + j\kappa_2 a_y - \sqrt{\gamma_{x_2}\gamma_{x_1}}a_{x_1} + j\sqrt{\gamma_{x_2}}E_x^{in}, \end{aligned} \tag{3}$$

$$\begin{aligned} j\omega a_y &= (j\omega_y - \gamma_y - \Gamma_y)a_y \\ &\quad + j\kappa_1 a_{x_1} + j\kappa_2 a_{x_2} + j\sqrt{\gamma_y}E_y^{in}. \end{aligned} \tag{4}$$

Here, $\kappa_1$ is the coupling coefficient between $a_{x_1}$ and $a_y$, $\kappa_2$ is the coupling coefficient between $a_{x_2}$ and $a_y$, $\omega_i$ $(i = x_1, x_2, y)$ are the resonance frequencies, $\gamma_i$ $(i = x_1, x_2, y)$ represent the radiative losses, and $\Gamma_i$ $(i = x_1, x_2, y)$ represent the dissipative losses. $E_x^{out}$ ($E_y^{out}$) and $E_x^{in}$ ($E_y^{in}$) are the $x$ ($y$) components of the output and input electric fields, respectively. The corresponding Hamiltonian matrix is[27]

$$H = \begin{pmatrix} \gamma_{x_2}\gamma_y\Delta\omega_{x_1} + j\gamma_{x_2}\gamma_y X_{x_1} & j\gamma_{x_1}\gamma_{x_2}\gamma_y & \kappa_1\sqrt{\gamma_{x_1}}\gamma_{x_2}\sqrt{\gamma_y} \\ j\gamma_{x_1}\gamma_{x_2}\gamma_y & \gamma_{x_1}\gamma_y\Delta\omega_{x_2} + j\gamma_{x_1}\gamma_y X_{x_2} & \kappa_2\gamma_{x_1}\sqrt{\gamma_{x_2}}\sqrt{\gamma_y} \\ \kappa_1\sqrt{\gamma_{x_1}}\gamma_{x_2}\sqrt{\gamma_y} & \kappa_2\gamma_{x_1}\sqrt{\gamma_{x_2}}\sqrt{\gamma_y} & \gamma_{x_1}\gamma_{x_2}\Delta\omega_y + j\gamma_{x_1}\gamma_{x_2}X_y \end{pmatrix}. \tag{5}$$

Here, $\Delta\omega_i = \omega_i - \omega$, and $X_i = \gamma_i + \Gamma_i$ $(i = x_1, x_2, y)$. To elucidate the physical essence of the EP, it is important to note that the primary propagation path for the system's energy among the three modes is $a_{x_1} \leftrightarrow a_y \leftrightarrow a_{x_2}$. The occurrence of the EP is primarily determined by the relative dissipation between the $x$-direction modes, $a_{x_1}$ or $a_{x_2}$, and the $y$-direction mode, $a_y$. The combination of gold and chromium is intentionally engineered to establish two distinct coupling channels within the metasurface. The first channel, positioned between the gold split-ring resonator and the metal bar $(a_{x_1} \leftrightarrow a_y)$, utilizes the same material and primarily depends on the tunable properties of $VO_2$ to identify the EP. The second channel, located between the chromium split-ring resonator and the metal bar $(a_y \leftrightarrow a_{x_2})$, incorporates both gold and chromium — materials characterized by significantly different conductivities. This design choice is specifically aimed at introducing a substantial inherent loss imbalance into the system, thereby facilitating a broad tuning range for the $VO_2$-based modulation. The dual-channel configuration is essential for realizing multiple second-order EPs within a single metasurface. Consequently, the aforementioned three-mode system can be equivalently transformed into a second-order non-Hermitian system with two main coupled modes, either $(a_{x_1}, a_y)$ or $(a_{x_2}, a_y)$. This transformation facilitates a clearer understanding of the intrinsic behavior of the EP. The dynamical equations for this system are referenced Refs. [25,30]:

$$\frac{\mathrm{d}a_x}{\mathrm{d}t} = (\mathrm{j}\omega_x - \gamma_x - \Gamma_x)a_x + \mathrm{j}\kappa a_y + \mathrm{j}\sqrt{\gamma_x}E_x^{\mathrm{in}}, \tag{6}$$

$$\frac{\mathrm{d}a_y}{\mathrm{d}t} = (\mathrm{j}\omega_y - \gamma_y - \Gamma_y)a_y + \mathrm{j}\kappa a_x + \mathrm{j}\sqrt{\gamma_y}E_y^{\mathrm{in}}. \tag{7}$$

The relationship between the transmitted field and the incident field of the metasurface can be expressed as

$$\begin{pmatrix} E_x^{\mathrm{out}} \\ E_y^{\mathrm{out}} \end{pmatrix} = \begin{pmatrix} E_x^{\mathrm{in}} \\ E_y^{\mathrm{in}} \end{pmatrix} + \begin{pmatrix} \mathrm{j}\sqrt{\gamma_x}a_x \\ \mathrm{j}\sqrt{\gamma_y}a_y \end{pmatrix}, \tag{8}$$

$$\begin{pmatrix} E_x^{\mathrm{out}} \\ E_y^{\mathrm{out}} \end{pmatrix} = \begin{pmatrix} t_{xx} & t_{xy} \\ t_{yx} & t_{yy} \end{pmatrix} \begin{pmatrix} E_x^{\mathrm{in}} \\ E_y^{\mathrm{in}} \end{pmatrix} = T \begin{pmatrix} E_x^{\mathrm{in}} \\ E_y^{\mathrm{in}} \end{pmatrix}. \tag{9}$$

To facilitate the determination of the system's Hamiltonian matrix, we multiply Eq. (6) by $\sqrt{\gamma_x}\gamma_y$ and Eq. (7) by $\gamma_x\sqrt{\gamma_y}$, yielding the following equations:

$$\begin{pmatrix} \gamma_y(\omega_x - \omega) + \mathrm{j}\gamma_y(\gamma_x + \Gamma_x) & \kappa\sqrt{\gamma_x\gamma_y} \\ \kappa\sqrt{\gamma_x\gamma_y} & \gamma_x(\omega_y - \omega) + \mathrm{j}\gamma_x(\gamma_y + \Gamma_y) \end{pmatrix} \begin{pmatrix} \mathrm{j}\sqrt{\gamma_x}a_x \\ \mathrm{j}\sqrt{\gamma_y}a_y \end{pmatrix} = -\mathrm{j}\gamma_x\gamma_y \begin{pmatrix} E_x^{\mathrm{in}} \\ E_y^{\mathrm{in}} \end{pmatrix}. \tag{10}$$

The Hamiltonian matrix H of the metasurface system can be expressed as[31,32]

$$H = \begin{pmatrix} \gamma_y(\omega_x - \omega) + \mathrm{j}\gamma_y(\gamma_x + \Gamma_x) & \kappa\sqrt{\gamma_x\gamma_y} \\ \kappa\sqrt{\gamma_x\gamma_y} & \gamma_x(\omega_y - \omega) + \mathrm{j}\gamma_x(\gamma_y + \Gamma_y) \end{pmatrix}. \tag{11}$$

Considering the zero detuning condition, $\Delta\omega_{x,y} = \omega_{x,y} - \omega = 0$, the Hamiltonian matrix can be further simplified to

$$H = \begin{pmatrix} \mathrm{j}\gamma_y(\gamma_x + \Gamma_x) & \kappa\sqrt{\gamma_x\gamma_y} \\ \kappa\sqrt{\gamma_x\gamma_y} & \mathrm{j}\gamma_x(\gamma_y + \Gamma_y) \end{pmatrix}. \tag{12}$$

The transmission matrix $T$ is related to the Hamiltonian matrix by $T = I - \mathrm{j}\gamma_x\gamma_y H^{-1}$. By solving the eigenvalues of T, it is found that when $|\gamma_y\Gamma_x - \gamma_x\Gamma_y| = 2\sqrt{\gamma_x\gamma_y}|\kappa|$, the two eigenvalues and their corresponding eigenvectors become degenerate simultaneously, thereby enabling the observation of the EP phenomenon.[24,25] In this study, the conductivity of $VO_2$ is modulated by external stimuli, which directly influences the dissipative loss $\Gamma_x$ of the resonator mode. Given that the unit cell inherently introduces a loss imbalance, adjusting the conductivity of $VO_2$ allows for precise control of $|\gamma_y\Gamma_x - \gamma_x\Gamma_y|$. Additionally, the coupling coefficient, $\kappa(\omega)$, is frequency-dependent. Therefore, the EP condition $|\gamma_y\Gamma_x - \gamma_x\Gamma_y| = 2\sqrt{\gamma_x\gamma_y}|\kappa(\omega)|$ can be conceptualized as the intersection between a horizontal line defined by conductivity and a frequency-dependent curve. At varying conductivities, the intersection frequencies correspond to distinct EPs. By systematically varying the conductivity, we identified three unique EPs at different frequencies, thus achieving controllable multi-frequency exceptional points.

## 3. Results and discussion

To numerically demonstrate the existence of multiple EPs in our designed $VO_2$-based actively tunable THz non-Hermitian metasurface device, we maintained the resonance frequencies of three components — two split-ring resonators and one metallic rod — around 1 THz by adjusting the openings of the split-ring resonators and the length of the metallic rod. Simulations were conducted using CST software over a frequency range of 0.6–1.3 THz, with $VO_2$ conductivity $(\sigma)$ varying from 100 $\mathrm{S{\cdot}m^{-1}}$ to 10,000 $\mathrm{S{\cdot}m^{-1}}$. The complex eigenvalues, phases, and corresponding eigenstates of the device were extracted using the frequency-domain solver and subsequently analyzed.

The simulation results indicate that as the conductivity of $VO_2$ $(\sigma)$ increases, the metasurface exhibits three instances of simultaneous degeneracy of eigenvalues and eigenstates within the frequency range of 0.6–1.3 THz, as illustrated in Fig. 2. The eigenvalues and eigenvectors of the transmission matrix characterize the inherent transmission response of the metasurface. Each eigenvalue $\lambda$ corresponds to a com-

plex transmission coefficient associated with a specific polarization eigenstate, where $|\lambda|$ and $\arg(\lambda)$ represent amplitude modulation and phase delay, respectively. The corresponding eigenvectors define the polarization states that remain invariant during the transmission process, even under non-Hermitian coupling. In the CST simulations, the scattering coefficients $t_{xx}$, $t_{xy}$, $t_{yx}$, and $t_{yy}$ are extracted and used to construct the transmission matrix, thereby obtaining the eigen decomposition of the transmission matrix through numerical methods. At the EP, two eigenvalues and their eigenvectors coalesce, indicating that the metasurface supports only a single circularly polarized eigenmode. As shown in Figs. 2(c), 2(f), 2(i)), this feature state degeneracy directly confirms the conditions for polarization singularity and the emergence of EPs with $2\pi$ phase winding. Specifically, at $VO_2$ conductivities of 3461 S·m$^{-1}$, 3950 S·m$^{-1}$, and 5534 S·m$^{-1}$, the metasurface demonstrates degenerate eigenvalue spectrum characteristics near 0.7725 THz, 1.2045 THz, and 1.08 THz, respectively. At these frequencies, the complex eigenvalues obtained from solving the non-Hermitian Hamiltonian of the metasurface show near-degeneracy in their real parts, imaginary parts, and phases. Consequently, the corresponding eigenstates degenerate into left-handed circular polarization (LCP) states, thereby satisfying the classical criteria for non-Hermitian EPs.

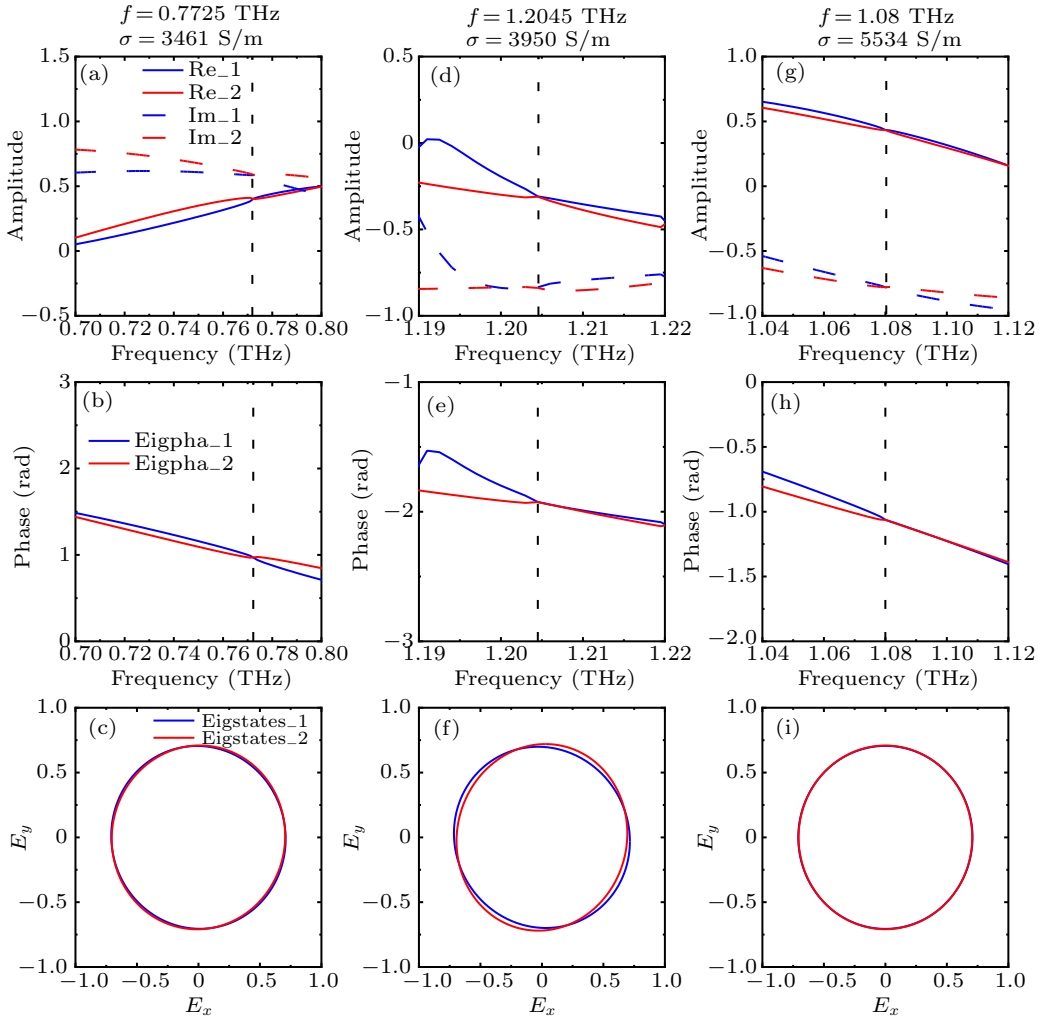



**Fig. 2.** Eigenvalues, phases, and eigenstates of the three EPs. Eigenvalue (a), phase (b), and eigenstate (c) at a frequency of 0.7725 THz and conductivity of 3461 S·m$^{-1}$. Eigenvalue (d), phase (e), and eigenstate (f) at a frequency of 1.2045 THz and conductivity of 3950 S·m$^{-1}$. Eigenvalue (g), phase (h), and eigenstate (i) at a frequency of 1.08 THz and conductivity of 5534 S·m$^{-1}$.

Non-Hermitian metasurfaces demonstrate a pronounced selectivity towards circular polarization states at the EP.[33] To elucidate their polarization-dependent behavior, we begin with the linear polarization basis and construct the complete transmission matrix. By employing the fundamental matrix formula $\Lambda = \frac{1}{\sqrt{2}}\begin{pmatrix} 1 & \mathrm{i} \\ 1 & -\mathrm{i} \end{pmatrix}$, we achieve the transformation from the linear polarization basis to the circular polarization basis, resulting in the circular polarization transmission matrix $T_{\mathrm{cir}}$:[34]

$$\begin{aligned} T_{\mathrm{cir}} &= \begin{pmatrix} t_{\mathrm{LL}} & t_{\mathrm{LR}} \\ t_{\mathrm{RL}} & t_{\mathrm{RR}} \end{pmatrix} \\ &= \frac{1}{2}\begin{pmatrix} t_{xx}+t_{yy}-\mathrm{i}\,(t_{xy}-t_{yx}) & t_{xx}-t_{yy}+\mathrm{i}\,(t_{xy}+t_{yx}) \\ t_{xx}-t_{yy}-\mathrm{i}\,(t_{xy}+t_{yx}) & t_{xx}+t_{yy}+\mathrm{i}\,(t_{xy}-t_{yx}) \end{pmatrix}. \end{aligned} \tag{13}$$

The transmission coefficient $t_{ij}$ represents the transmission from $j$-polarized incident light to $i$-polarized outgoing light. The subscripts L and R denote LCP and right circularly polarized light (RCP), respectively, while the subscripts $x$ and $y$ represent $x$-polarized light and $y$-polarized light. As shown in Fig. 3(a), within the frequency range of 0.6–1.3 THz, the active modulation of the conductivity of $VO_2$ causes the incident light at three EP frequency points to collapse two orthogonal eigenstates into circularly polarized states. Furthermore, after passing through the metasurface, the incident circularly polarized light retains only the LCP component in the outgoing wave, while the RCP component is almost completely suppressed, achieving chiral selective transmission. By utilizing Eq. (13), the cross-polarized $t_{RL}$ transmission spectra at the three EP points are calculated, as illustrated in Fig. 3(b). The results show that under the conductivity conditions of 3461 S·m$^{-1}$, 3950 S·m$^{-1}$, and 5534 S·m$^{-1}$, the cross-polarized transmission curves $t_{RL}$ of the metasurface circularly polarized light exhibit transmission minima at the corresponding EP frequencies (0.7725 THz, 1.2045 THz, and 1.08 THz), indicating that the energy conversion pathway from LCP to RCP is effectively suppressed.

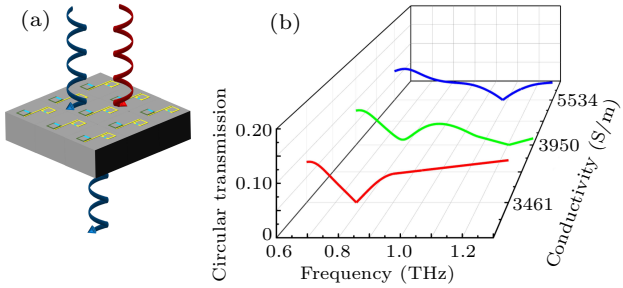



**Fig. 3.** Response of the metasurface to circularly polarized light. (a) Schematic illustration of the asymmetric transmission of circularly polarized light through the metasurface. (b) Transmission coefficients when the incident wave is LCP and the outgoing wave is right-handed circularly polarized (RCP) at different conductivities.

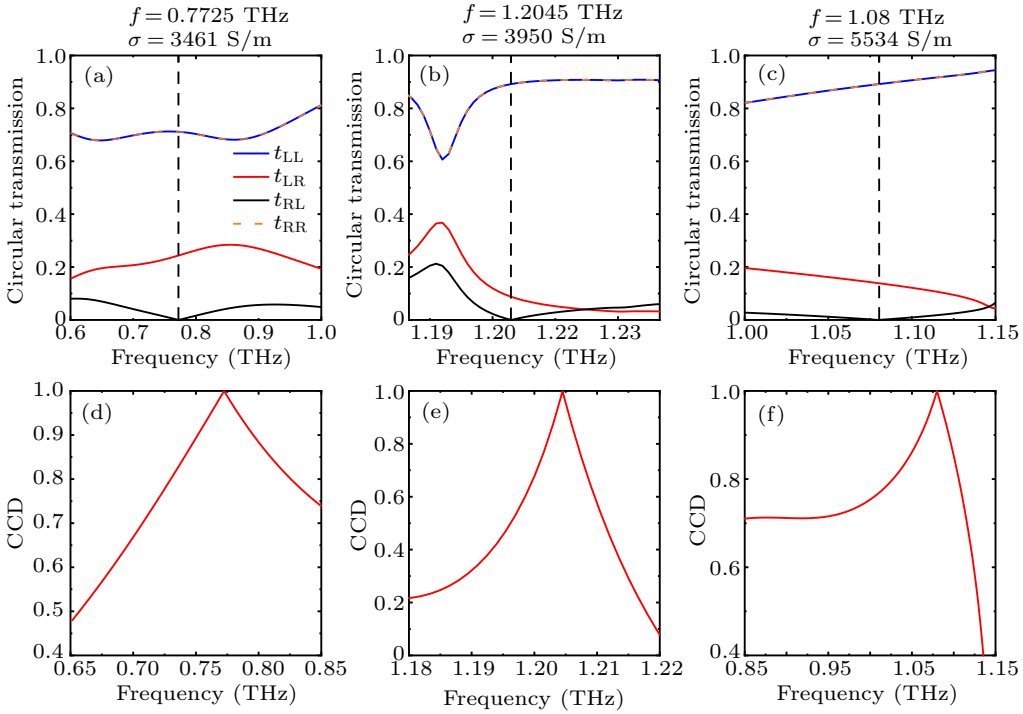



**Fig. 4.** Transmission spectra and circularly converted dichroism (CCD) corresponding to the three EPs. Transmission spectrum (a) and CCD (d) at a frequency of 0.7725 THz and conductivity of 3461 S·m$^{-1}$. Transmission spectrum (b) and CCD (e) at a frequency of 1.2045 THz and conductivity of 3950 S·m$^{-1}$. Transmission spectrum (c) and CCD (f) at a frequency of 1.08 THz and conductivity of 5534 S·m$^{-1}$.

As shown in Figs. 4(a)–4(c), simulations reveal that the cross-polarization channel $t_{RL}$ approaches zero at the three EP frequencies, leading to the near-complete disappearance of the conversion channel from LCP to RCP light, while the cross-polarization channel $t_{LR}$ is far from zero, and the co-polarization channels $t_{LL}$ and $t_{RR}$ are both non-zero. This indicates that the eigenstates of the non-Hermitian metasurface are degenerate to LCP at the EP frequencies. Interestingly, the designed metasurface exhibits a disappearance of the conversion channel from LCP to RCP at the three EPs. Consequently, we calculated the circularly converted dichroism (CCD) at the three EPs, defined as CCD $= (t_{LR} - t_{RL})/(t_{LR} + t_{RL})$.[35] Figures 4(d)–4(f) show that the CCD values at the frequency points of the three EPs are all greater than 0.99. This result indicates that the metasurface structure achieves nearly complete transmission of LCP and strong suppression of RCP under EP conditions, demonstrating excellent chiral filtering capabilities, which have potential applications in scenarios involving asymmetric transmission and polarization control.

The EP in non-Hermitian systems differs from the double-cone degeneracy topology found in Hermitian systems, exhibiting a unique topological structure within the parame-

ter space where complex eigenvalues connect across two Riemann sheets.[36] Figure 5 illustrates the topological evolution of the modulus (a)–(c) and phase (d)–(f) of the complex eigenvalues in the parameter space, corresponding to three frequencies (0.7725 THz, 1.2045 THz, and 1.08 THz), as functions of $VO_2$ conductivity and frequency. It is clearly observed that the red and blue surfaces undergo degeneracy at a specific point in the parameter space (marked by the yellow dot), indicating that the system enters the EP state and forms the characteristic Riemann sheets. This structure directly reflects the topological dependence of non-Hermitian dynamics. Thus, the Riemann sheet structure serves as a key characteristic of EPs.

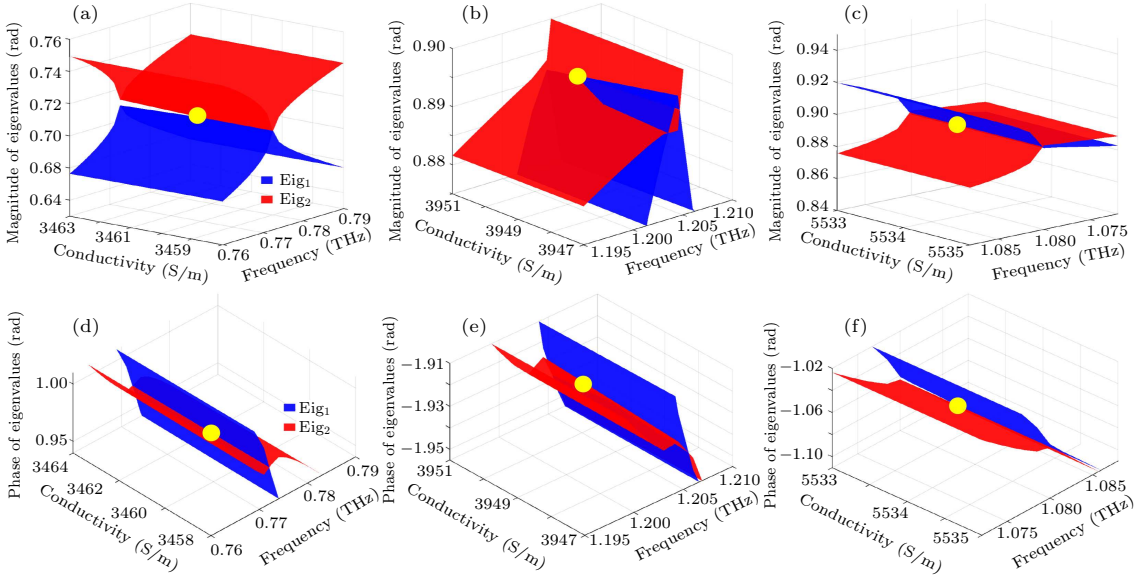



**Fig. 5.** Eigenvalues and phase surfaces in the parameter space formed by conductivity and frequency, calculated from simulation data. Panels (a)–(c) are the eigenvalue surfaces around the three EP parameter points $(\sigma, f) = (3461\ \mathrm{S\cdot m^{-1}}, 0.7725\ \mathrm{THz})$, $(3950\ \mathrm{S\cdot m^{-1}}, 1.2045\ \mathrm{THz})$, and $(5534\ \mathrm{S\cdot m^{-1}}, 1.08\ \mathrm{THz})$, respectively. Panels (d)–(f) are the corresponding phase surfaces. The blue and red sheets represent the first and second eigenvalue branches, respectively, with the yellow dots marking the locations of the respective EPs.

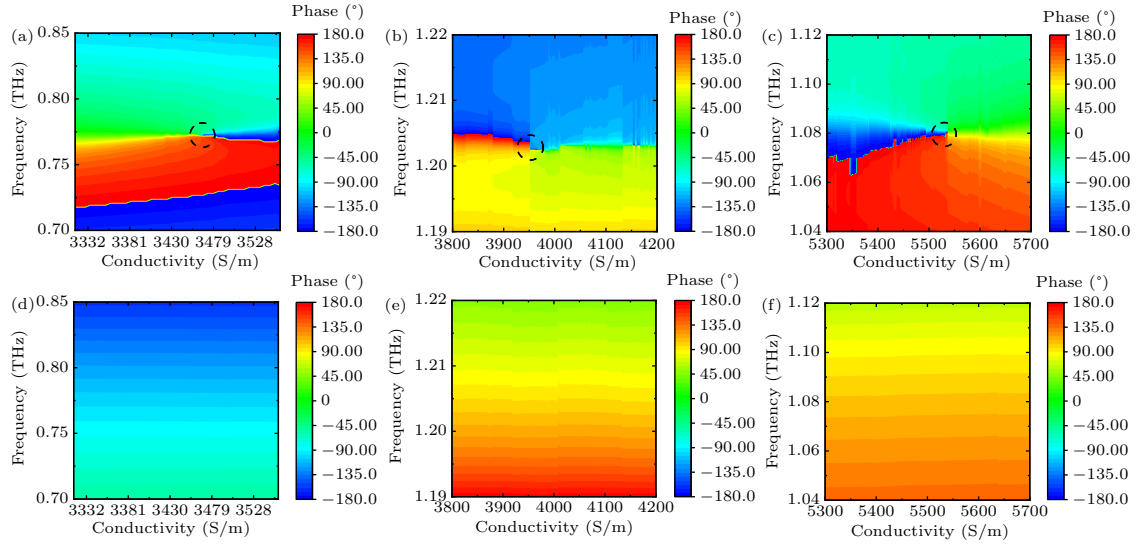



**Fig. 6.** Topological protection of the metasurface. Phase distributions of (a) $t_{\mathrm{RL}}$ and (d) $t_{\mathrm{LR}}$ in the parameter space where the EP occurs at $(\sigma, f) = (3461\ \mathrm{S\cdot m^{-1}}, 0.7725\ \mathrm{THz})$. Phase distributions of (b) $t_{\mathrm{RL}}$ and (e) $t_{\mathrm{LR}}$ in the parameter space where the EP occurs at $(\sigma, f) = (3950\ \mathrm{S\cdot m^{-1}}, 1.2045\ \mathrm{THz})$. Phase distributions of (c) $t_{\mathrm{RL}}$ and (f) $t_{\mathrm{LR}}$ in the parameter space where the EP occurs at $(\sigma, f) = (5534\ \mathrm{S\cdot m^{-1}}, 1.08\ \mathrm{THz})$. The black circles in (a)–(c) indicate the $2\pi$ phase accumulation around the EP.

To further elucidate the topological characteristics of the system at the EPs, we conducted an in-depth analysis of the phase distributions for the two cross-circular polarization channels, $t_{\mathrm{RL}}$ and $t_{\mathrm{LR}}$. When the system satisfies the EP condition, the LCP to RCP conversion channel virtually disappears, i.e., $t_{\mathrm{RL}} = 0$, indicating that an EP forms a phase singularity in this channel. Figure 6 presents the phase distributions of the two channels, $t_{\mathrm{RL}}$ and $t_{\mathrm{LR}}$, in the two-dimensional parameter space $(\sigma, f)$ for three EP parameter points, specifically $(\sigma, f) = (3461\ \mathrm{S\cdot m^{-1}}, 0.7725\ \mathrm{THz})$, $(3950\ \mathrm{S\cdot m^{-1}}, 1.2045\ \mathrm{THz})$, and $(5534\ \mathrm{S\cdot m^{-1}}, 1.08\ \mathrm{THz})$. Figures 6(a)–6(c) correspond to the $t_{\mathrm{RL}}$ channel, where a clear $2\pi$ phase winding structure centered around the EP can be observed. This is a typical topological phase accumulation phenomenon

in non-Hermitian systems. In contrast, as shown in the $t_{LR}$ channel in Figs. 6(d)–6(f), the RCP to LCP conversion channel does not exhibit a similar phase singularity, and its phase distribution remains continuous and smooth throughout the parameter space. This asymmetry suggests that a $2\pi$ singular phase accumulation occurs only in the specific channel satisfying the EP condition, while the other direction maintains conventional behavior. Unlike conventional Pancharatnam–Berry (PB) phases, this $2\pi$ phase transition arising around the EP possesses topological robustness: a $2\pi$ accumulation is invariably generated as long as the path encircles the EP, irrespective of the path's shape. This characteristic holds significant importance for topological photonic devices and ultra-sensitive phase sensing.

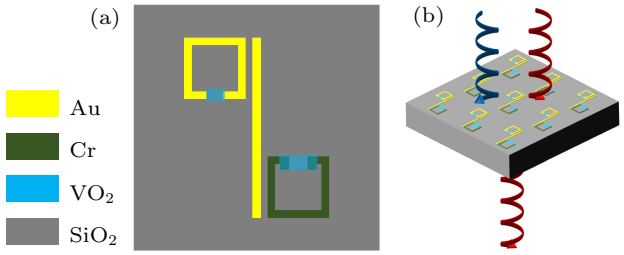



**Fig. 7.** (a) Top view of the unit cell structure of the mirror metasurface. (b) Schematic illustration of asymmetric transmission under circularly polarized light incidence.

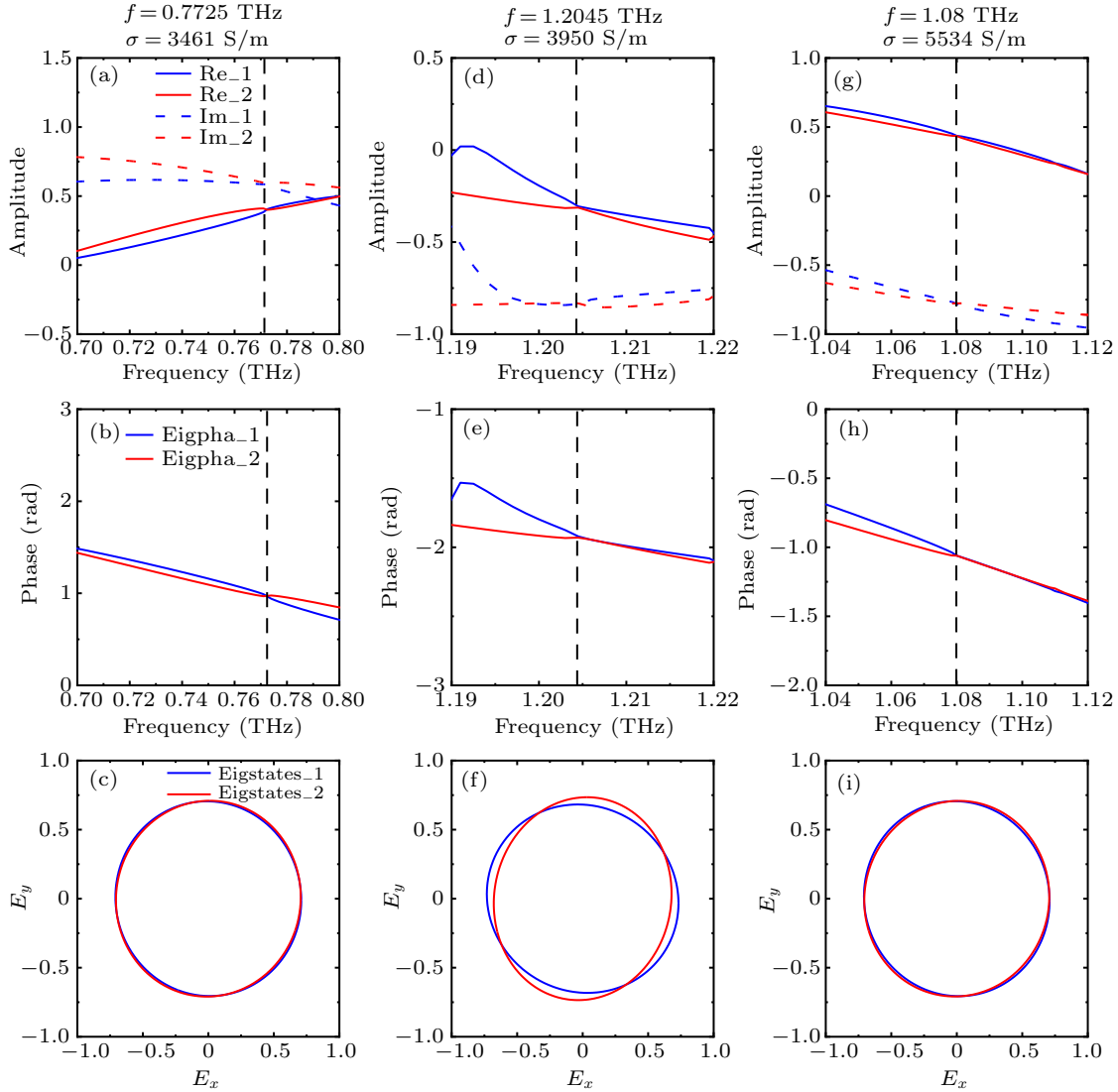



**Fig. 8.** Eigenvalues, phases, and eigenstates of the three EPs in the mirror metasurface. At a frequency of 0.7725 THz and a conductivity of 3461 S·m$^{-1}$: (a) eigenvalues, (b) phases, (c) eigenstates. At a frequency of 1.2045 THz and a conductivity of 3950 S·m$^{-1}$: (d) eigenvalues, (e) phases, (f) eigenstates. At a frequency of 1.08 THz and a conductivity of 5534 S·m$^{-1}$: (g) eigenvalues, (h) phases, (i) eigenstates.

Due to the geometric configuration of the designed mirror metasurface, which cannot perfectly coincide with the original structure through arbitrary spatial rotations or translations, the structure exhibits geometric chirality. As illustrated in Fig. 7(a), this structural chirality provides a unique platform for analyzing polarization-selective behaviors in non-Hermitian systems. To investigate its chiral response characteristics, we actively tuned the mirror structure at different $VO_2$ conductivities and compared its EP characteristics with those of the original metasurface. Based on the simu-

lated transmission data, we extracted the eigenvalues, eigenstates, and phase distributions of the mirror metasurface under various tuning parameters, as shown in Fig. 8. The simulation results demonstrate that the mirror metasurface satisfies the EP conditions at the following parameter points: when $(\sigma, f) = (3461\ \mathrm{S\cdot m^{-1}}, 0.7725\ \mathrm{THz})$, the real and imaginary parts of the system's two eigenvalues are completely degenerate at 0.7725 THz, with corresponding phases being equal, and the eigenstates degenerating into circular polarization states. When $(\sigma, f) = (3950\ \mathrm{S\cdot m^{-1}}, 1.2045\ \mathrm{THz})$ and $(5534\ \mathrm{S\cdot m^{-1}}, 1.08\ \mathrm{THz})$, complete degeneracy of eigenvalues and phases also occurs at the respective frequency points, with eigenstates degenerating into circular polarization states in both cases. These results indicate that, through active tuning of the $VO_2$ conductivity, EPs emerge at three points in the parameter space: $(3461\ \mathrm{S\cdot m^{-1}}, 0.7725\ \mathrm{THz})$, $(3950\ \mathrm{S\cdot m^{-1}}, 1.2045\ \mathrm{THz})$, and $(5534\ \mathrm{S\cdot m^{-1}}, 1.08\ \mathrm{THz})$. Notably, compared to the LCP eigenstates corresponding to EPs in the original metasurface, the mirror structure entirely degenerates into RCP eigenstates at EPs under the same parameter conditions. This significant difference highlights the crucial role of structural chirality in determining the handedness of EP eigenstates. Simultaneously, this phenomenon confirms the chirality sensitivity and structural controllability of non-Hermitian singular points within the polarization space.

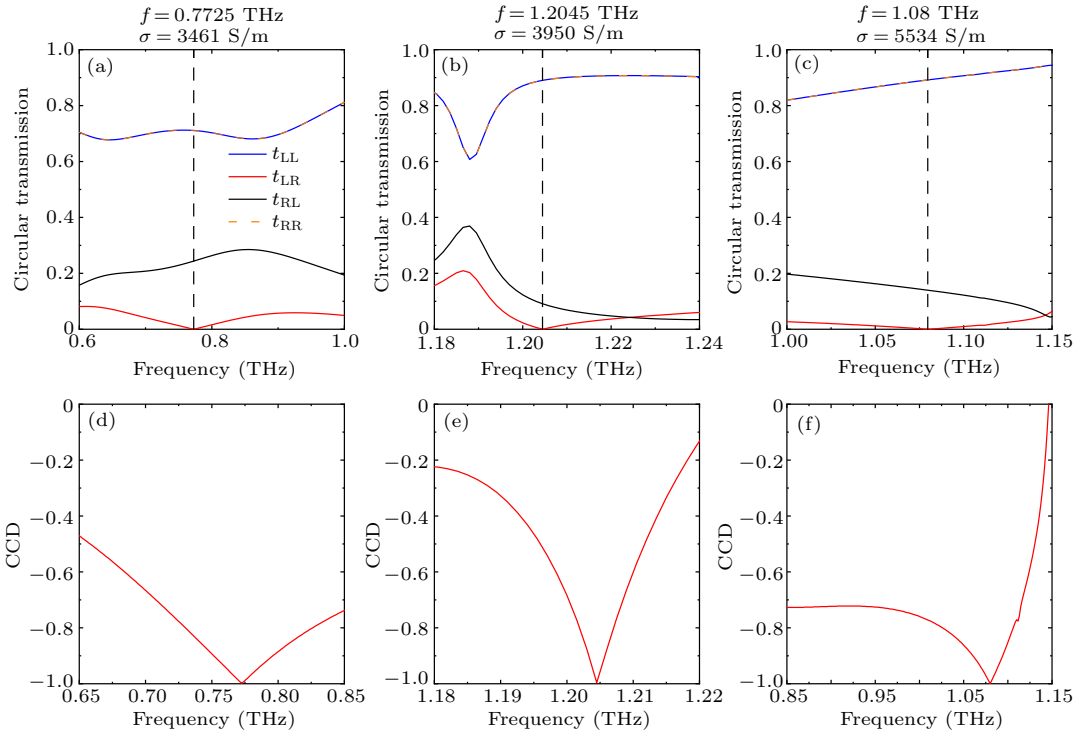



**Fig. 9.** Transmission spectra and circularly converted dichroism (CCD) of the mirror metasurface. For the mirror metasurface at a frequency of 0.7725 THz and a conductivity of 3461 $\mathrm{S\cdot m^{-1}}$: (a) transmission spectrum and (d) CCD. For the mirror metasurface at a frequency of 1.2045 THz and a conductivity of 3950 $\mathrm{S\cdot m^{-1}}$: (b) transmission spectrum and (e) CCD. For the mirror metasurface at a frequency of 1.08 THz and a conductivity of 5534 $\mathrm{S\cdot m^{-1}}$: (c) transmission spectrum and (f) CCD.

According to Eq. (13), we calculated the transmission spectra of the system under three EP parameter conditions: $(\sigma, f) = (3461\ \mathrm{S\cdot m^{-1}}, 0.7725\ \mathrm{THz})$, $(3950\ \mathrm{S\cdot m^{-1}}, 1.2045\ \mathrm{THz})$, and $(5534\ \mathrm{S\cdot m^{-1}}, 1.08\ \mathrm{THz})$, as illustrated in Figs. 9(a)–9(c). The figures reveal that the co-polarized transmission, $t_{\mathrm{LL}} = t_{\mathrm{RR}} \neq 0$, indicates a strong retention capability of the LCP and RCP states along their intrinsic directions. Conversely, the cross-polarized transmission shows $t_{\mathrm{LR}} = 0$, while $t_{\mathrm{RL}} \neq 0$, demonstrating significant asymmetric transmission characteristics for circular polarization. Specifically, as depicted in Fig. 7(b), in the mirror metasurface, when the incident wave is LCP, the transmitted wave is RCP. Conversely, when the incident wave is RCP, the LCP output is nearly completely suppressed, indicating that the conversion pathway from RCP to LCP is inhibited. In contrast, the original metasurface (Fig. 3(a)) exhibits an opposite unidirectional polarization conversion response: the conversion pathway from LCP to RCP is suppressed, while the conversion from RCP to LCP is preserved. This mirror-symmetric circular polarization transmission behavior indicates that non-Hermitian EP states exhibit an inversion characteristic of the eigenstate chirality under varying structural chiralities. By comparing the transmission spectra shown in Figs. 4(a)–4(c) (original metasurface structure) with those in Figs. 9(a)–9(c) (mirror metasurface structure), it is further confirmed that at the EP, the original metasurface selectively suppresses the conversion pathway from LCP to RCP, whereas the mirror structure suppresses the conversion pathway from RCP to LCP. This be-

havior clearly reflects the high sensitivity of the EP response to structural geometric chirality. The circularly converted dichroism (CCD) values at the three EPs are calculated and displayed in Figs. 9(d)–9(f), all of which are less than −0.99, indicating that the system nearly achieves complete retention of RCP transmission while strongly suppressing the LCP transmission output at these EPs. This highly asymmetric transmission behavior not only reveals the chirality-sensitive characteristics of the EP states but also underscores the potential application value of this structure in constructing novel circular polarization selectors, chiral filters, and other devices.

The proposed $VO_2$–Au/Cr hybrid metasurface can be readily fabricated using standard micro-nanofabrication techniques. The fabrication process begins with spin-coating a positive photoresist onto a cleaned $SiO_2$ substrate, followed by ultraviolet photolithography to define the patterns of the gold and chromium split-ring resonators along with the central metallic rod. A thin adhesion layer of chromium is deposited first, followed by a gold film, both via electron-beam evaporation. The unwanted metal is then removed through a lift-off process in acetone, leaving behind the designed metallic structures. Following this, a second lithography step is employed to define the $VO_2$ deposition areas located in the gaps of the resonators. Amorphous $VO_2$ thin films are deposited by magnetron sputtering under low-temperature conditions and subsequently crystallized through rapid thermal annealing in an inert atmosphere to achieve phase-change $VO_2$ with tunable conductivity. For experimental characterization, a terahertz time-domain spectroscopy (THz-TDS) system equipped with polarization control can be utilized. By measuring the four complex transmission coefficients ($t_{xx}$, $t_{xy}$, $t_{yx}$, and $t_{yy}$) under different $VO_2$ states, the complete transmission matrix can be reconstructed. The eigenvalues and eigenvectors of the transmission matrix are calculated to identify the frequencies and conductivity conditions where both coalesce, corresponding to the occurrence of EPs. The conductivity of $VO_2$ can be dynamically adjusted either through thermal tuning, where the sample is mounted on a temperature-controlled micro-heating stage to facilitate the insulator-metal transition, or via optical pump-THz probe excitation, in which femtosecond laser irradiation induces an ultrafast and reversible change in conductivity. These approaches provide a practical means for experimentally observing and validating the multi-frequency EPs predicted in this study.

## 4. Conclusions

This work presents a THz non-Hermitian metasurface featuring actively tunable multi-frequency EPs based on $VO_2$. By embedding $VO_2$ thin films at the apertures of two split-ring resonators and continuously tuning their conductivity, the system's dissipation is independently controlled under fixed geometric dimensions, achieving simultaneous degeneracy of the real and imaginary parts of the eigenvalues, phase, and eigenstates across three discrete frequency bands. This allows observation of multi-frequency EPs on a single metasurface. Upon the occurrence of EPs, the device exhibits unidirectional polarization conversion characteristics for circularly polarized THz waves: the original metasurface structure suppresses the LCP to RCP conversion, whereas the mirror metasurface structure suppresses the RCP to LCP conversion, with corresponding circularly converted dichroism (CCD) values reaching +0.99 and −0.99, respectively. This chiral inversion indicates that the eigenstate helicity of the EP is determined by geometric mirroring, highlighting the high sensitivity of the non-Hermitian spectrum to structural chirality. Further analysis reveals that encircling any EP along a path in parameter space results in a $2\pi$ topological phase accumulation, confirming the predicted Riemann sheet topological characteristics. Therefore, this study leverages the reversible dissipation tuning provided by the $VO_2$ phase transition to realize and manipulate EPs across multiple frequency bands without altering the metasurface dimensions. This offers new design paradigms for non-Hermitian topological optics and chiral polarization control, while also laying a theoretical foundation for the development of multifunctional THz integrated devices.

## Acknowledgements

This work was supported by the National Natural Science Foundation of China (Grant No. 62375158), the Qingdao Natural Science Foundation (Grant No. 25-1-1-153-zyyd-jch), and the Development Plan of Youth Innovation Team in Colleges and Universities of Shandong Province (Grant No. 2022KJ216).

## References

[1] Bender C M and Boettcher S 1998 *Phys. Rev. Lett.* **80** 5243
[2] Wong Z J, Xu Y L, Kim J, O'Brien K, Wang Y, Feng L and Zhang X 2016 *Nat. Photon.* **10** 796
[3] Zhu S Y, Wu G B, Pang S W and Chan C H 2022 *Adv. Opt. Mater.* **10** 2101663
[4] Samizadeh Nikoo M and Matioli E 2023 *Nature* **614** 451
[5] Rüter C E, Makris K G, EI-Ganainy R, Christodoulides D N, Segev M and Kip D 2010 *Nat. Phys.* **6** 192
[6] Gupta S K, Zou Y, Zhu X Y, Lu M H, Zhang L J, Liu X P and Chen Y F 2020 *Adv. Mater.* **32** 1903639
[7] Li J Y, Fu J, Liao Q and Ke S L 2019 *J. Opt. Soc. Am. B* **36** 2492
[8] Özdemir Ş K, Rotter S, Nori F and Yang L 2019 *Nat. Mater.* **18** 783
[9] Li A, Wei H, Cotrufo M, Chen W J, Mann S, Ni X, Xu B C, Chen J F, Wang J, Fan S H, Qiu C W, Alù A and Chen L 2023 *Nat. Nanotechnol.* **18** 706
[10] Ding X S, Liu W Y, Wang S X, Tao Y, Zhou Y R, Bai Y, Liu L, Xing E B, Tang J and Liu J 2024 *Chin. Phys. B* **33** 084204
[11] Ding K, Ma G, Xiao M, Zhang Z Q and Chan C T 2016 *Phys. Rev. X* **6** 021007
[12] Xiao Z C, Li H N, Kottos T and Alù A 2019 *Phys. Rev. Lett.* **123** 213901
[13] Hodaei H, Hassan A U, Wittek S, Garcia-Garcia H, El_Ganainy R, Christodoulides D N and Khajavikhan M 2017 *Nature* **548** 187
[14] Park J H, Ndao A, Cai W, Hsu L Y, Kodigala A, Lepetit T, Lo Y H and Kante B 2020 *Nat. Phys.* **16** 462

[15] Kim J, Ha T, Kim D, Lee D, Lee K S, Won J, Moon Y and Lee M 2023 *Appl. Phys. Lett.* **123** 161104
[16] Müller M and Rotter I 2008 *J. Phys. A: Math. Theor.* **41** 244018
[17] Guo A and Salamo G J 2009 *Phys. Rev. Lett.* **103** 093902
[18] Lin Z, Ramezani H, Eichelkraut T, Kottos T, Cao H and Christodoulides D N 2011 *Phys. Rev. Lett.* **106** 213901
[19] Sun Y, Tan W, Li H Q, Li J and Chen H 2014 *Phys. Rev. Lett.* **112** 143903
[20] Longhi S 2010 *Phys. Rev. A* **82** 031801
[21] Zhang S M, He T Y and Jin L 2024 *Chin. Phys. Lett.* **41** 027201
[22] Holloway C L, Dienstfrey A, Kuester E F, O'Hara J F, Azad A K and Taylor A J 2009 *Metamaterials* **3** 100
[23] Liu C, Lan J, Gu Z M and Zhu J 2023 *Chin. Phys. Lett.* **40** 124301
[24] Lawrence M, Xu N, Zhang X Q, Cong L Q, Han J G, Zhang W L and Zhang S 2014 *Phys. Rev. Lett.* **113** 093901
[25] Li S X, Zhang X Q, Xu Q, Liu M, Kang M, Han J G and Zhang W L 2020 *Opt. Express* **28** 20083
[26] He W B, Hu Y Z, Ren Z H, Hu S Y, Yu Z Y, Wan S, Cheng X A and Jiang T 2023 *Adv. Sci.* **10** 2304972
[27] Li S M, Chao T, and Gilardi C, *et al.* 2023 *International Electron Devices Meeting*, December 9–13, 2023, San Francisco, USA, p. 1
[28] Wen Q Y, Zhang H W, Yang Q H, Xie Y S and Chen K 2010 *Appl. Phys. Lett.* **97** 021111
[29] Dong X X, Luo X Q, Zhou Y X, Lu Y F, Hu F R, Xu X L and Li G Y 2020 *Opt. Express* **28** 30675
[30] Fan S H, Suh W and Joannopoulos J D 2003 *J. Opt. Soc. Am. A* **20** 569
[31] Jin B B, Tan W, Zhang C H, Wu J B, Chen J, Zhang S and Wu P H 2018 *Adv. Theo. Sim.* **1** 1800070
[32] Tan W, Zhang C H, Li C, Zhou X Y, Jia X Q, Feng Z, Su J and Jin B B 2017 *Appl. Phys. Lett.* **110** 181111
[33] Li Z K, Yang W K, Jiang C Y, Sang X T, Wang J, Lv X Y, Zhang H Y and Zhang Y P 2023 *Phys. Chem. Chem. Phys.* **25** 6510
[34] Li J Y, Fu J, Liao Q and Ke S L 2019 *J. Opt. Soc. Am. B* **36** 2492
[35] Zhang Y P, Liu Y, Wang Y, Zheng S Y and Hao X Y 2025 *J. Appl. Phys.* **137** 053102
[36] Park S H, Lee S G, Baek S, Ha T, Lee S, Min B, Zhang S, Lawrence M and Kim T T 2020 *Nanophotonics* **9** 1031